Influence of Marshalling Length on Aerodynamic Characteristics of Urban Emus under Crosswind

H. Liang[1], Y. Sun[2], T. Li[1†] and J. Zhang[1]

[1] State Key Laboratory of Traction Power, Southwest Jiaotong University, Chengdu 610031, China
[2] China National Accreditation Center for Conformity Assessment, Beijing 100062, China

[†]Corresponding Author Email: litian2008@home.swjtu.edu.cn

ABSTRACT

Urban electric multiple units (EMUs) is based on high-speed trains and metro vehicle technology. Their design speeds are generally from 160km/h to 200km/h, which mitigates the low operating speeds of metro vehicles. Traditional crosswind calculations for the aerodynamic characteristics of trains often assume a 3-marshalling train. Urban trains are generally 4-marshalling and 6-marshalling. Evaluating the aerodynamic characteristics of urban EMUs of different marshalling lengths is instructive for system design. Based on CFD, aerodynamic models of urban trains are established. The train models include 3-marshalling, 4-marshalling and 6-marshalling. The aerodynamic characteristics of 200km/h urban trains subject to different crosswind velocities are numerically simulated. The research display that the aerodynamic performance of the head-car and the first middle-car, under the same crosswind velocity, of different marshalling lengths, are almost the same, whereas the aerodynamic characteristics of the tail-cars for different marshalling lengths are significantly different. The side forces of the 4 middle-cars of the 6-marshalling train decrease, sequentially. At a crosswind velocity of 35m/s, 34% difference in F_s of the tail-car of a 6-marshalling train compared to a 3-marshalling, and the overturning moment differs by 22.8%. Because of the significant difference in side force and overturning moment, the three-marshalling train model cannot represent the real train. Therefore, the real marshalling length should be used, as far as possible, when studying crosswind effects on the train.

Keywords: Crosswind; Marshalling length; Train aerodynamics; Urban trains; Numerical simulation.

NOMENCLATURE

D	outer windshield length	***V***	velocity vector
F_d	aerodynamic drag	*ρ*	air density
S	generalized source term	**Φ**	general variable
t	time variable	**Γ**	air density

1. INTRODUCTION

At present, research on high-speed railway equipment in China has mainly focused on safety, reliability, economy, environmental protection, and intelligence (Qi and Zhou 2020). High-speed trains are being actively developed to be greener, more energy-saving, and faster (Tian 2019). Urban railway is a new type of passenger rail transportation in metropolitan areas. It not only has the advantages of large passenger capacity, quick starting and stopping, fast boarding and alighting, etc., but also some advantages of high-speed EMUs, such as high speed and comfort (Zhang *et al.* 2017; Li *et al.* 2021). During the operation of municipal EMUs,

crosswinds are the most frequently encountered operating condition, and strong crosswind significantly affect the train operation. Chang *et al.* (2022) discovered that size played a significant role in the train resistance in crosswind.

Generally, the real length of high-speed trains is 8 or 16 marshalling, and urban EMUs is 4 or 6 marshalling. However, combined with wind tunnel tests feasibility and the numerical calculation efficiency, researchers usually use 3-marshalling train for research. However, the aerodynamic performance of short trains and long trains are quite different.

Therefore, scholars research how the marshalling lengths affects the outflow field around train under different conditions. Jia *et al.* (2017) study how train length influences the wake flow. The results show that the longer the train length, the worse the wake symmetry. Muld *et al.* (2014) studied the relationship of train length and wake structures, based on DDES. To better understand induced flow, Bell *et al.* (2014) studied how the wake of the tail-car are affected by L/h. This work was a first step towards understanding the interaction between L/H ratio and train slipstream. Ricco *et al.* (2007) studied the changes of pressure waves when trains of different lengths passing through the tunnel, by employing a moving model test. They found that the pressure wave of long trains changed more significantly and lasted longer. Martínez *et al.* (2008) reached the same conclusion, using full-scale tests. Liu *et al.* (2019) researched how the number and length of train formation affected the train aerodynamic performance when train passing through the tunnel. They found that there was a intense interaction between the marshalling length and the pressure fluctuations of the train. Mohebbi and Rezvani (2018) investigated how the height and type of air fences affects the rolling moment of train.

In general, researchers have mainly focused on the effect of different marshalling lengths on the wake structures, and changes in the pressure fluctuations of the train under different conditions. However, few studies have mentioned how the marshalling length affects the train under crosswind. So, under crosswind conditions, the impact of marshalling length on the aerodynamic characteristics of urban EMUs is carried out. The aerodynamic force, aerodynamic moment, surface pressure, flow field velocity distribution and flow field comparison of different marshalling lengths under crosswind are analyzed in-depth. This work provides a reference for the operational safety of urban EMUs in a crosswind environment.

2. METHODOLOGY

Fluid flow must satisfy the three laws of conservation in physics. They are mass conservation, momentum conservation and energy conservation, which can be expressed by the equation of continuity, the equation of momentum, and the equation of energy in mathematics. The following is the general governing equation.

$$\frac{\partial \rho \boldsymbol{\Phi}}{\partial t} + \mathrm{div}\rho \boldsymbol{V}\boldsymbol{\Phi} = \mathrm{div}(\boldsymbol{\Gamma}\,\mathrm{grad}\boldsymbol{\Phi}) + S$$

where $\boldsymbol{\Phi}$ is a general variable; $\boldsymbol{V}$ is the velocity vector; t is the time variable; $\boldsymbol{\Gamma}$ is the general diffusion coefficient; ρ is the density; S is the generalized source term.

When numerical calculations are performed for the flow around the train, the selection of a suitable turbulence model is crucial. The Reynolds average method is the most widely used method for numerical calculation of turbulence flows (Li *et al.* 2018; Li *et al.* 2019). So, the 3-dimensional, steady and incompressible Navier-stokes equation and SST k-ω two equation turbulence model are developed (Raithby and Schneider 1979). And the SST k-ω turbulence model is more conducive to solving for the boundary layer flow at the surface of a train (Patankar 1985).

In this research, we performed the solution of the simulation by using ANSYS FLUENT 15.0. One Inter(R) Xeon(R) Platinum 8269CY (2.5GHz) processor with 48 cores and 128G is used to perform the calculation. It takes 240 hours to complete the calculation of all working conditions. The continuity residual is required to be below 10^{-3}, and the other residuals are required to be below 10^{-4}.

3. COMPUTATIONAL MODEL

3.1 Train Model

In this study, a urban EMUs model was used as research object. The train marshalling form is composed of the head-car, middle-car and tail-car. Figure 1 exhibit the train formation. The number of middle-car is N. N is taken as 1, 2, and 4, giving marshalling numbers of 3, 4, and 6 cars. The train model is illustrated in Fig. 2. Take the 3-car marshalling model as an example, lights, door handles, pantographs and other parts are ignored, while parts such as the bogie area and bogies are retained. Figure 3 display the computation domain and the size of computation domain. The distance from the head-car nose to the Inlet1 is 100 m, and the distance from the tail-car nose to the Outlet2 is 200 m. Both sizes exceed the minimum requirements specified in EN14067-6 (2010).
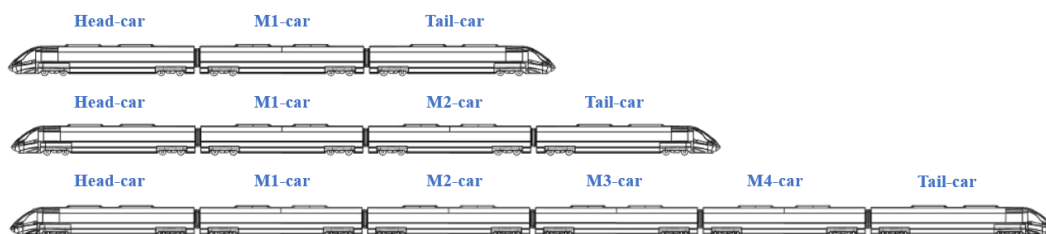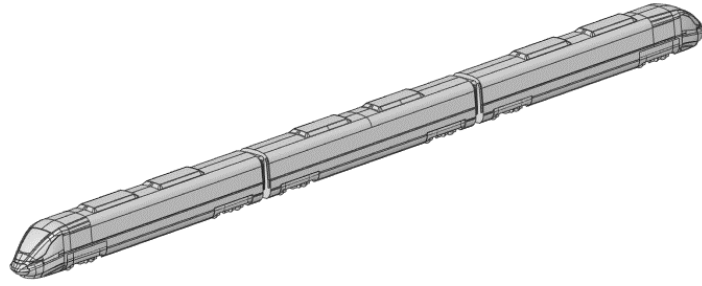

Fig. 1. Train formation.
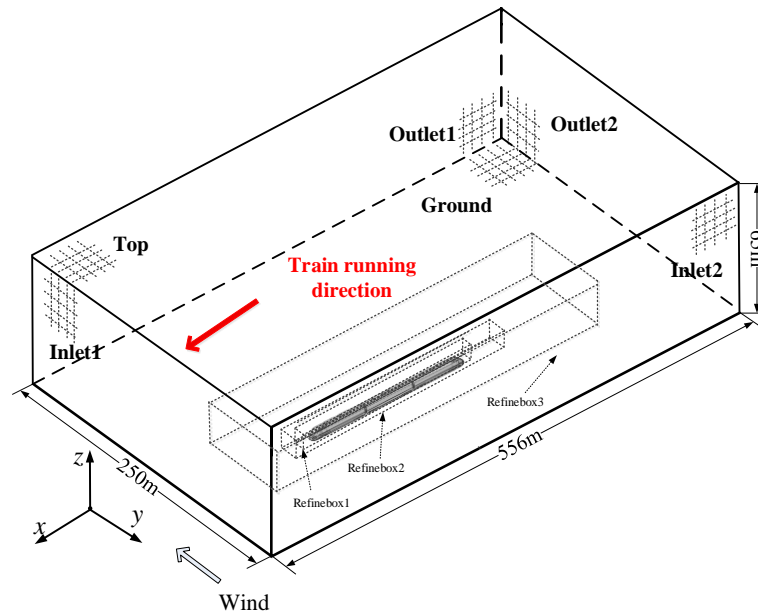
Fig. 2. Train model.

Fig. 3. Computational domain.

3.2 Computational Information

The boundary conditions are set as follows: Inlet1 and Inlet2 are set as velocity inlets. The direction of train running is *x* direction, the velocity in *x* direction is 55.56m/s. The velocity in *y* direction is the crosswind velocity, which is 15, 20, 25 ,30 and 35m/s, for different tests. Outlet1 and outlet2 are set as the pressure outlets. Top is the symmetry condition. Ground is the slip wall, with a velocity of 55.56m/s. The surface of train is the no-slip fixed wall.

This research focuses on how the train formation length affects the aerodynamic force and moment of each carriage, under cross wind. Steady-state calculation is enough to meet the needs of this paper. The SIMPLE algorithm is already extensively applied in the field of high-speed train calculation (Liu *et al.* 2018; Van Doormaal and Raithb, 1984).

3.3 Computational Mesh

In considering the effect of different spatial mesh structures on the results, three sets of grids of different sizes are created and numerically calculated. The mesh structure is shown in Fig. 4. Table 1 shows the calculation results of different grid sizes. We know from Table 1 that when using the second set of grids, the aerodynamic resistance on the train is 1.63% smaller than the first set of grids and 0.20% smaller than the third set of grids. It can be seen that if the grid size continues to be refined, the aerodynamic forces of the train is almost independent of the grid size. The second set of grids has met the requirements of grid independence. Therefore, the second set of grids is used for numerical simulation. The mesh structure is illustrated in Fig. 4. Figure 5 displays *y*+ diagram of the train. The boundary layer grid is divided at the train surface based on the consideration of the effects between the car body surface and the air flow. The thickness for the first layer has been set to 0.01 mm. Each set of grids has 12 boundary layers. Then, the grid growth ratio is set to 1.2.

Table 1. Calculation results using different grids.

Mesh	Numbers of mesh($\times 10^4$)	F_d (N)	Relative error （%）
Mesh1	1591	15064	—
Mesh2	2176	14818	1.63
Mesh3	3311	14848	0.20

(a) Grid around the train

(b) Grid of boundary layer   (c) Grid on the head-car
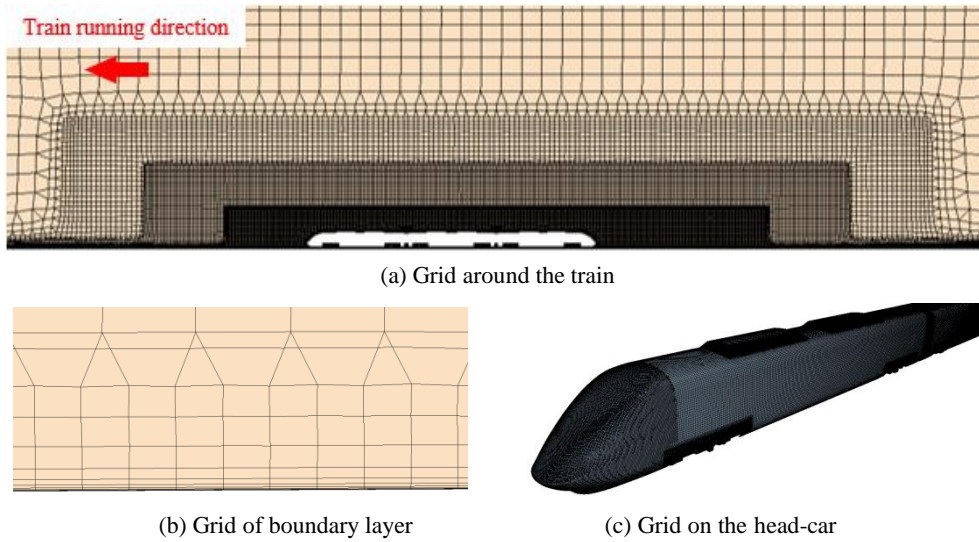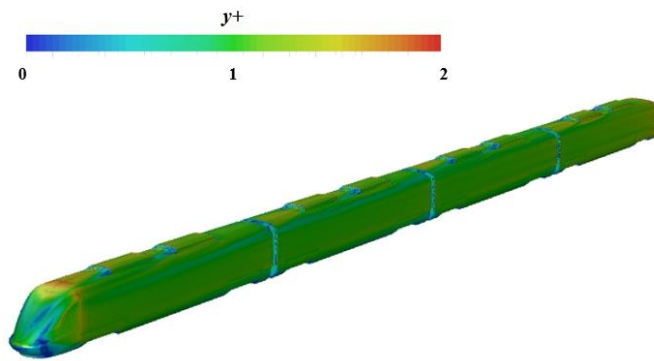
Fig. 4. Calculation mesh.
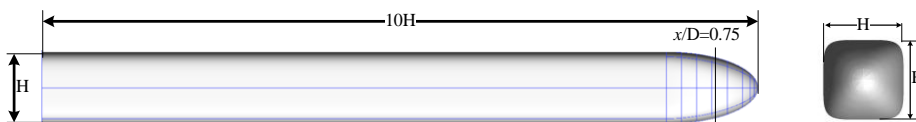

Fig. 5. *y*+ distribution of the train.

Fig. 6. Idealized train.

4. NUMERICAL VALIDATION

For the aim of verifying the accuracy and reliability of the calculation results, numerical simulations were carried out to demonstrate the accuracy of the train aerodynamic calculation. The idealized train model (Chiu and Squire 1992) is selected as the verification object. Figure 6 display the idealized model. The H is 125 mm. The x/D=0.75 section was extracted for subsequent verification. The position of the x/D=0.75 section is shown in Fig. 6(a).

The *x/*D=0.75 cross section of Chiu's test (Chiu and Squire 1992) was chosen for verification. Figure 7 shows the pressure values of the cross section compared to the Chiu's test. The extraction method for section pressure is consistent with that of Chiu's test. Comparing the numerical data with test data, we

know that the simulation results are in good agreement with the Chiu's result. It shows that the calculation method in this paper is reasonable.

5. RESULTS

The calculation results will be analyzed, looking at three main areas, being the aerodynamic force, pressure distribution and flow field.

5.1. Aerodynamic Force

The aerodynamic side forces (F_s) of trains at 15, 20, 25, 30 and 35m/s crosswind velocity of different marshalling lengths are shown in Fig. 8. Figure 8 show that the F_s on the each car increase of crosswind velocity when the marshalling length of the train is the same. When the crosswind velocity is the same, the F_s of head-car is biggest, the tail-car is
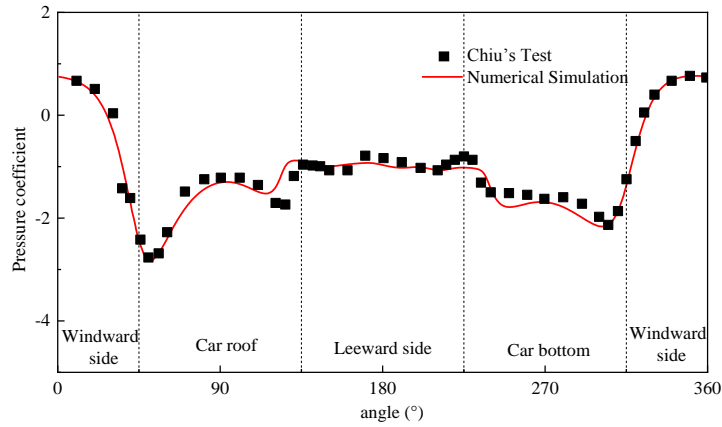
Fig. 7. Surface pressure distribution.

(a) F_s of each car of three marshalling train

(b) F_s of each car of six marshalling train
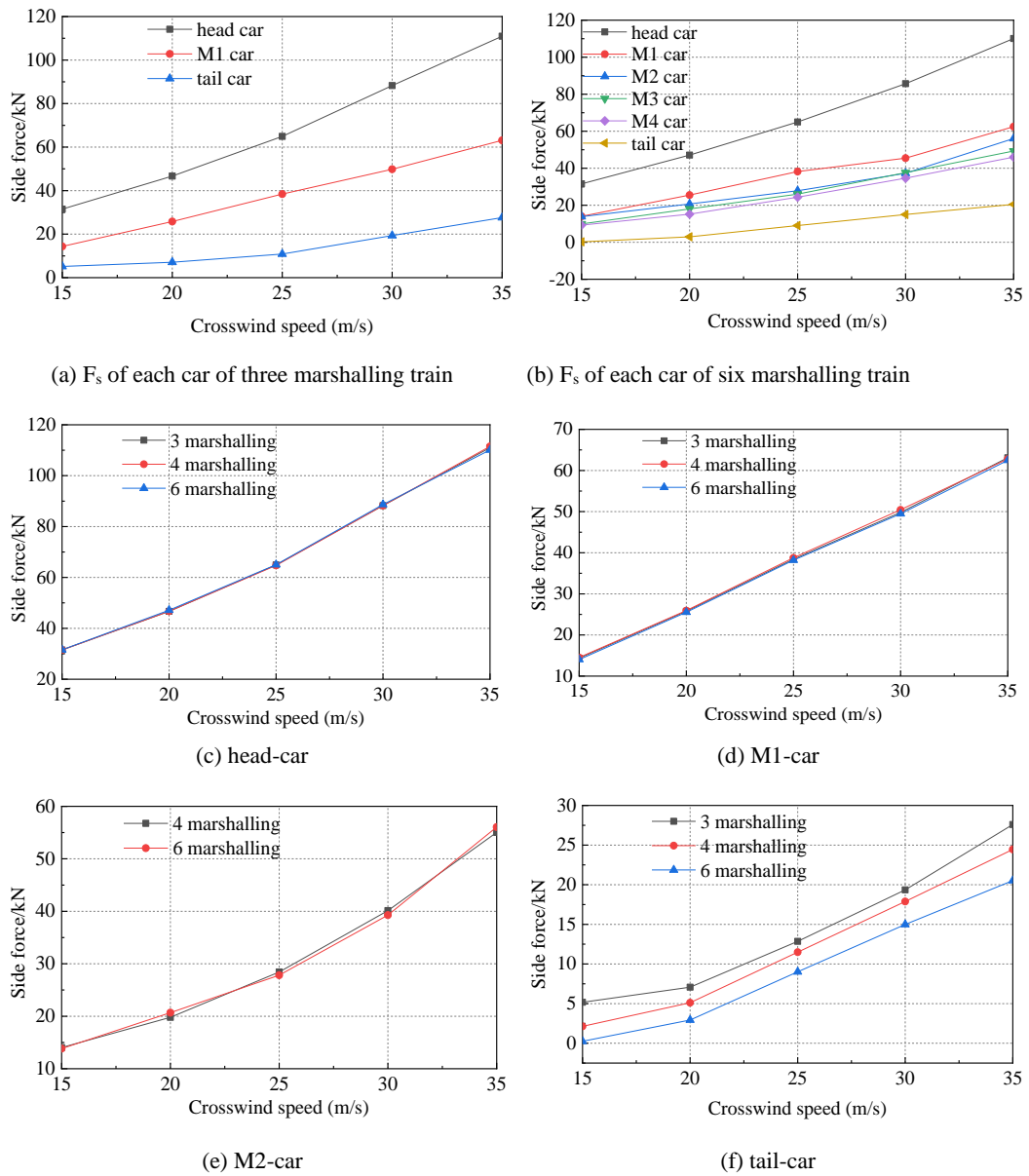
(c) head-car

(d) M1-car

(e) M2-car

(f) tail-car

Fig. 8. Influence of crosswind velocity and marshalling length on F_s of train.

smallest. When the train formation lengths are different, the head-car, M1-car and M2-car of 4 and 6 formations experience almost the same aerodynamic F_s, under the same crosswind velocity. Regardless of the marshalling length, the airflow formed by the running wind and the crosswind starts to be distributed around the train in the order of the head-car, M1-car, and the M2-car. Therefore, under the same train speed and crosswind velocity, the external flow field structure and F_s of the head-car, the M1-car and the M2-car of the 4 and 6 marshalling trains, are the same. This phenomenon is similar to conclusions in Guo's research (Guo *et al.* 2016). At the same crosswind velocity, the F_s of the tail-cars of different marshalling trains are obviously different.

Figure 9 shows the overturning moment (M_o) curves at 15, 20, 25, 30 and 35m/s crosswind velocity for trains of different marshalling lengths. We know that the M_o of each car with the same marshalling length,

increase with the increase of crosswind velocity. When the crosswind velocity is the same, the M_o of head-car is biggest, the tail-car is smallest. When the train formation lengths are different, the head-car, M1-car and M2-car of 4 and 6 marshalling trains have almost the same M_o, under the same crosswind velocity. At the same crosswind velocity, the marshalling length obviously affects the M_o of the tail-car. When the marshalling length increases. the M_o of the tail-car decreases.

5.2 Train Surface Pressure

Figure 10 shows the pressure distribution of the four middle-cars. The top row is car M1, the second, third and fourth rows are cars M2, M3 and M4 respectively. From Fig. 10, we know that the red rectangular box concentrates the maximum positive pressure. The maximum value of positive pressure shows a decreasing trend from top to bottom. The
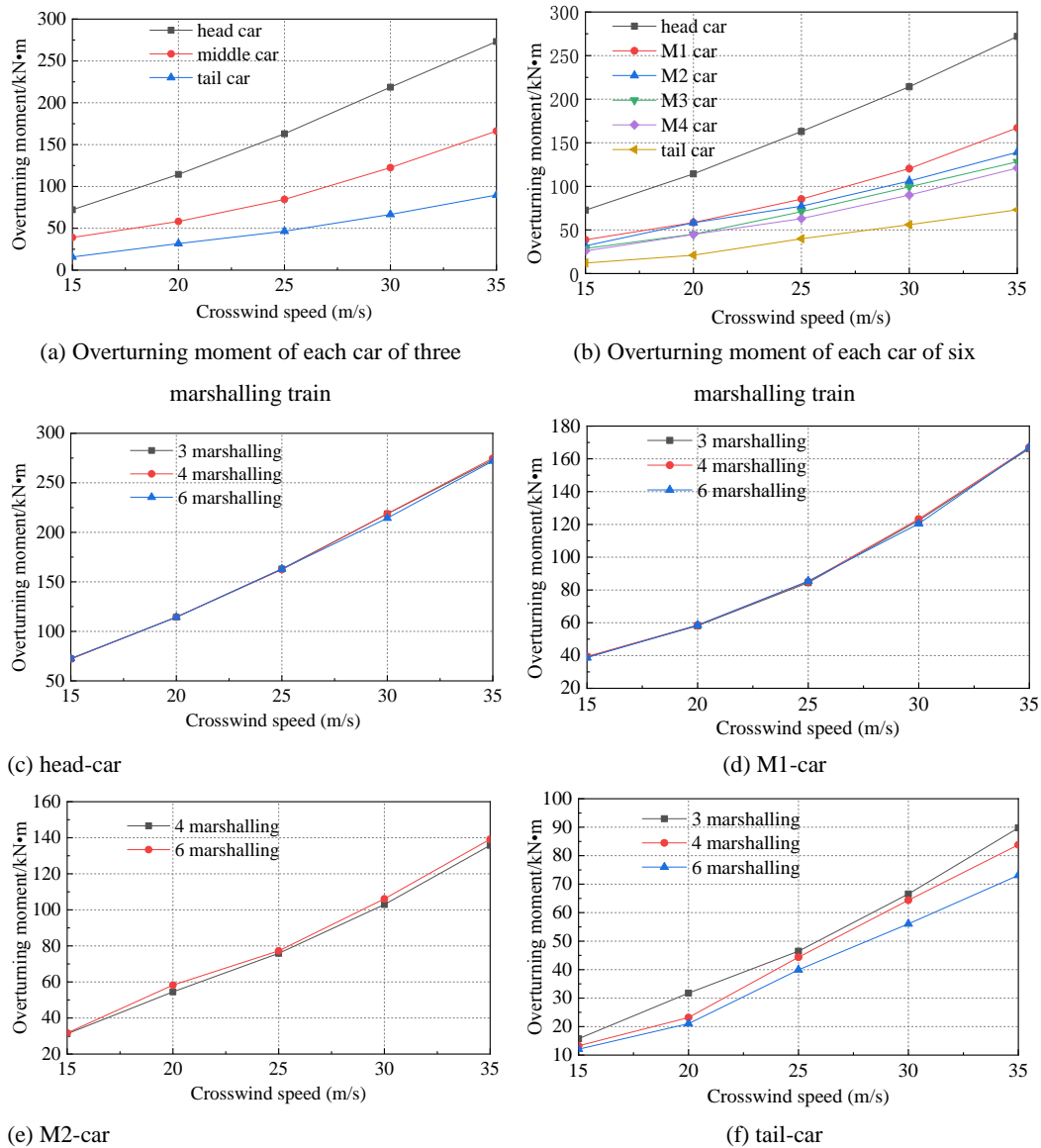
(a) Overturning moment of each car of three marshalling train

(b) Overturning moment of each car of six marshalling train

(c) head-car

(d) M1-car

(e) M2-car

(f) tail-car

Fig. 9. Influence of crosswind velocity and marshalling length on overturning moment of train.

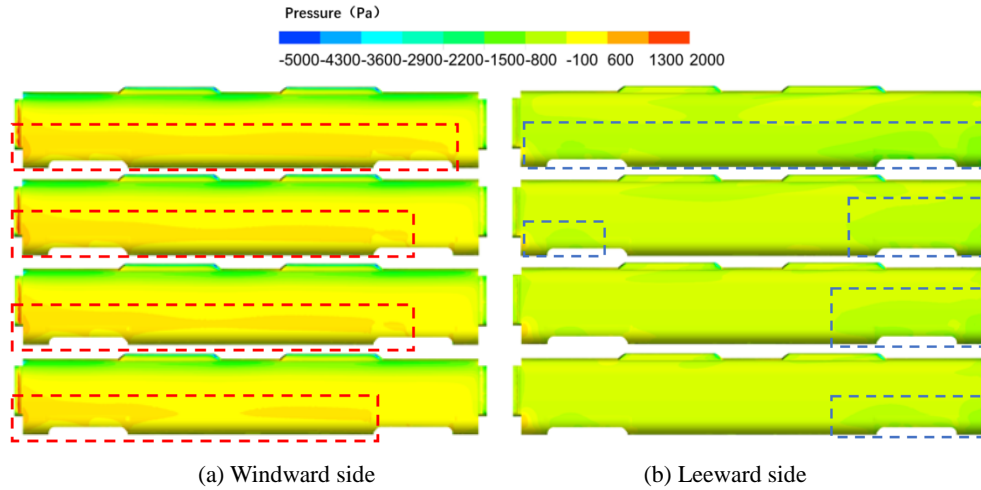(a) Windward side   (b) Leeward side

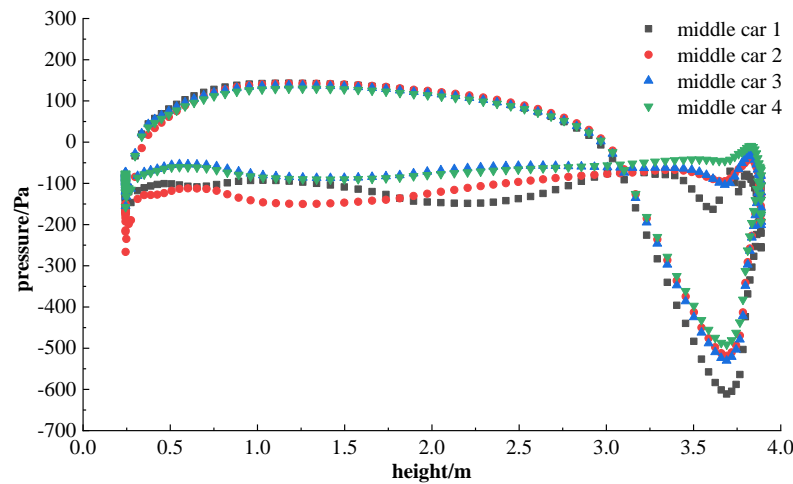**Fig. 10. Pressure distribution of the middle-car of 6-marshalling train.**

Fig. 11. Middle section pressure of 4 middle-cars of 6-marshalling train.

maximum negative pressure is primarily focused on the blue rectangular box. The positive pressure zone of the 4 middle-cars on the windward side decreases from the top row to the bottom. The laws on the leeward side are consistent. Compared with the windward side, the change is more pronounced on the leeward side. This is the reason that the F_s and M_o of the 4 middle-cars appears in Figs. 8(b) and 9(b)

To compare the difference in surface pressure of trains in detail, Fig. 11 show the mid-sections of the 4 middle-cars of 6-marshalling trains. We know from Fig. 11 that the cross-sectional pressure trends of the 4 middle-cars are roughly the same. There is little variation in surface positive pressure in the middle and lower areas (z=0.5~3m) of the windward side of the train. Because the upper area (z=3~3.9m) on the train is a rounded roof, the surface pressure first decreases sharply, the minimum negative pressure appearing at $z = 3.3$m, and then increases sharply. The change of M1-car is significantly greater than the other three middle-cars. This is probably due to

the complex flow field on the train, and there is vortex separation. From the M1-car to the M4-car, the surface negative pressure of the upper region z= (3~3.9m) on train decreases in order.

According to the above results, we know that the Fs and Mo of the tail-car are subject to the marshalling length. The boundary layer on the tail-car surface was extracted to explore how different marshalling lengths affect the tail-car. We know from Fig. 12 that the longer the marshalling length, the thicker the boundary layer. This is in line with the results in the paper (Bell *et al.* 2015). There are three abrupt changes of A, B and C near the windshield of the tail-car. B and C are caused by the front and rear of the bogie of the tail-car. The change of the A caused by the windshield Moreover, the three abrupt changes are largest with three-marshalling trains, and smallest with six-car trains.

5.3 Flow Structure

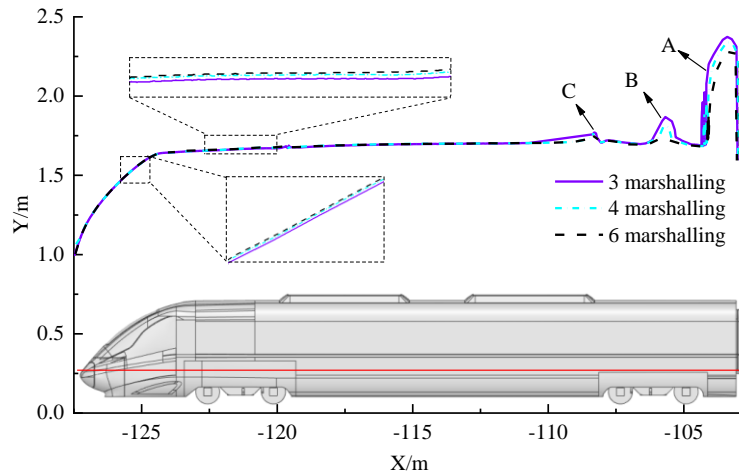Figure 13 displays the vortex structure of trains, and

Fig. 12. Surface boundary layer on windward side of tail-car with different marshalling length.
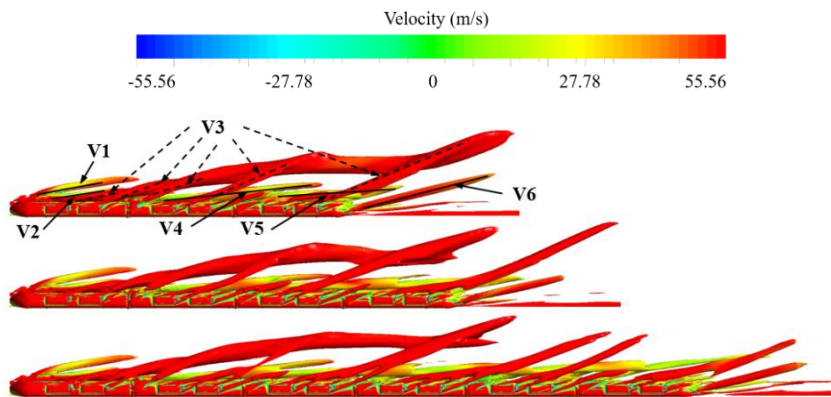

Fig. 13. Vortex structure of different marshalling trains.

it is colored based on air velocity. These vortex structures are mainly located on the leeward side of the train, due to the existence of crosswinds. Depending on the source and direction of vortices, they can be distinguished according to six main types of vortex structures: vortex V1 was developed from the head-car nose, moves backward at a certain angle with the car body, then gradually leave the train, finally disappearing at head-car windshield. Vortex V2 and V1 develop in the same position, but then the vortex V2 moves backwards, and disappears in the front half of the M1-car. The series of vortices V3 are caused by the airflow separation at the rear end of the air conditioner of each car. These vortices V3 are leave the train, at a certain angle. The front-end V3 will combine with the rear-end V3 during the backward development process, to form a larger combined vortex V3. The V4 is generated from the front of the M1-car, then moves backwards Vortex V5 is generated at the windshield of the tail-car, close to the tail-car body, develops backwards, and gradually disappears in the flow field. The vortex V6 is generated from the tail-car, caused by crosswind, at large angle to the car body, then disappears in the flow field.

Comparing the vortex structure, We know that the marshalling length has great influence on the vortex structure. but the vortex structures of V1, V2 and V4 are not influenced. Larger marshalling lengths cause the location where all V3 vortices combine to form a combined vortex, move backwards and the size of the combined vortex increase. As the marshalling length increases, the number of V3 also increases. Regardless of the marshalling length, the vortex V5 will develop close to the car body, disappearing at the tail-car. The generation position of V6 does not change with the marshalling length, but its strength decreases with the increase of the marshalling length The mid-sections (x=-22.8 m, -45.6 m, -68.4 m and -91.2 m) of the 4 middle-cars in 6-marshalling groups, are shown in Fig. 14. Figure 14(a) is the schematic diagram of four cross section locations. Analyzing the influence of different marshalling lengths on the vortex structure and velocity distribution, we know that significant differences exist in the streamline diagrams of the cross-sections in the four-section middle-car. First, the vortex shapes are quite different between the four cross-sections. We know that the velocity difference between the cross-sections of the 4 middle-cars is
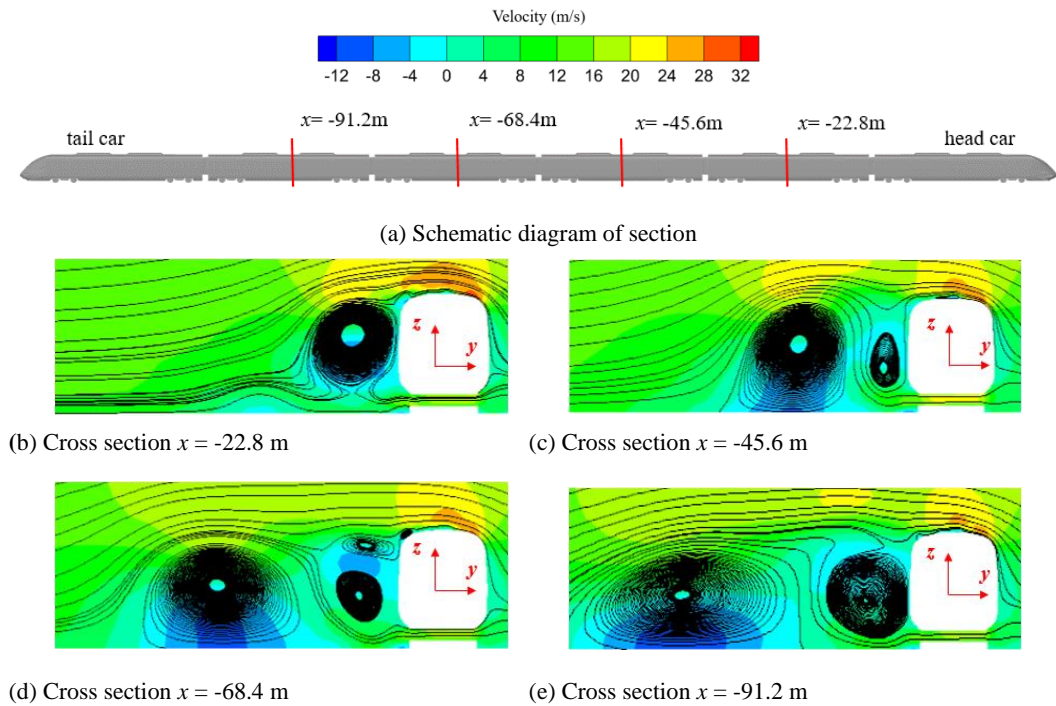
Velocity (m/s)

-12 -8 -4 0 4 8 12 16 20 24 28 32

tail car   *x* = -91.2m   *x* = -68.4m   *x* = -45.6m   *x* = -22.8m   head car

(a) Schematic diagram of section

(b) Cross section *x* = -22.8 m

(c) Cross section *x* = -45.6 m

(d) Cross section *x* = -68.4 m

(e) Cross section *x* = -91.2 m

Fig. 14. Diagram of velocity and flow in the middle section of 4 middle-cars of 6-marshalling train.

also relatively large, and the velocity at the top of the M1-car is higher, compared with the other three cars. The negative pressure on the windward side surface (z=3 ~ 3.9m) of the M1-car is bigger, compared to the other three intermediate cars, it is consistent with the variation law in Fig. 11. The middle and lower part of the windward side has the same incoming wind velocity and there is no vortex shedding. It could explain why the pressures of the 4 middle-cars are basically the same in the middle and lower areas (z=0.5~3m) of the train, depicted in Fig. 11.

The velocity distribution of 3-marshalling, 4-marshalling, 6-marshalling is shown in Fig. 15. The differences in velocity distribution are on the leeward side, and are mainly divided into three areas: A area, B area, and C area. When the same train running speed and crosswind velocity are used, different marshalling length has no effect on area A, which agrees with Fig. 8(c) and Fig. 9(c). When the marshalling length of the train increases, there is not

much difference in the area affected by the vortex V4 at the front end. However, there is a clear distinction in the area affected by the vortex V5 at the back end. When the marshalling length increases, the affected area at the end of the area B increases. Area C is influenced by the mixing of vortices V5 and V6. As the marshalling length increases, the impact of area C progressively increases, and V5 and V6 tend to combine.

Combining Figs. 13 and 15 for analysis, we found that the tail-car is mainly influenced from the V5 and V6. We know from Figure 15 that the strength of vortex V5 has weakened and is far away from the train, when it evolves at the tail-car, due to the increase of marshalling length. The vortex V6 decreases in strength when the marshalling length increases. This explains why, as the marshalling length increases, the F_s and M_o on the tail-car gradually decrease.

Velocity (m/s)

-55.56   -27.78   0   27.78   55.56
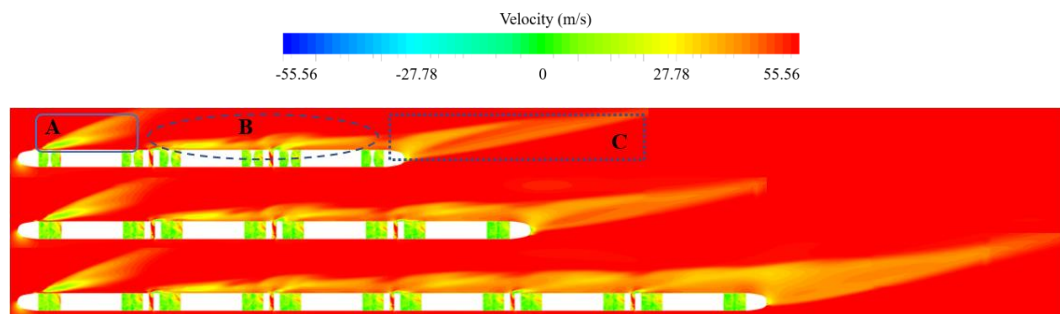
A   B   C

Fig. 15. Velocity distribution of horizontal section of trains of different marshalling length.

When the train is running in crosswind condition, the airflow separation phenomenon of the train body is more frequent. The airflow separation phenomenon at the tail-car is especially obvious. Figure 16 shows the velocity vector diagram of tail-car, for different marshalling lengths. It is clear that with the increase of marshalling length, the separation point at the tail-car nose gradually moves downward. The airflow separation phenomenon here is mainly caused by the interaction of the vortices V5 and V6 in Fig. 13, which again proves that as the length of the marshalling increases, the intensity of the vortex acting on the tail gradually decreases.

Figure 17 display the streamline diagram of the longitudinal section of the tail-car nose with different marshalling lengths. It can be seen that there are certain differences on the leeward side for different marshalling lengths. Vortices V3, V5, V6 and vortex Q, located at the lower part of the train nose, can be seen in this section. With the increase of train marshalling length, the vortices V3, V5, and

V6 gradually leave the car body, and gradually become bigger. When the train is 3-marshalling, the vortex Q is almost at the same height. When the marshalling length increases, the vortex Q near the windward side gradually develops upward, while the vortex Q near the leeward side gradually becomes larger.

From Fig. 13, we can observe the three-dimensional vorticity diagram surrounding the train. To further understand the vorticity distribution of car body, we extract the vorticity of the horizontal section (z=1m) of trains, which is illustrated in Fig. 18. From this we can see that the vortex distribution in the horizontal section is largely consistent with that in Fig. 13. The marshalling length will not affect the vortex distribution around the head-car and the first intermediate car. That is to say, V1, V2 and V4 are essentially the same. The development of V3 involves the confluence of many vortices, and the three groups of V3 in the section undergo little
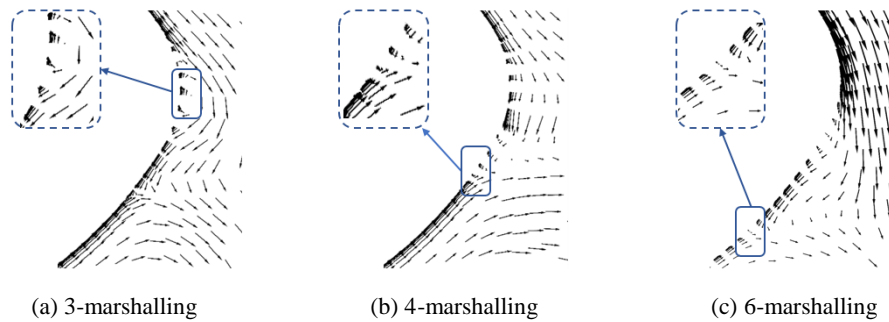

(a) 3-marshalling (b) 4-marshalling (c) 6-marshalling

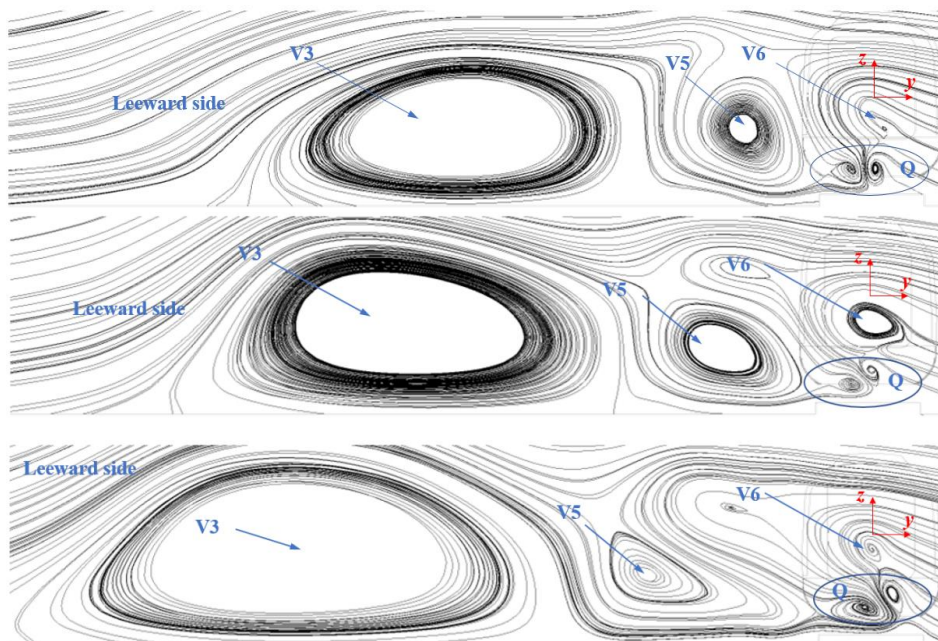**Fig. 16. Velocity vector distribution of nose of tail-cars with different marshalling.**

Fig. 17. Streamline distribution of longitudinal section of tail nose of trains with different marshalling length.
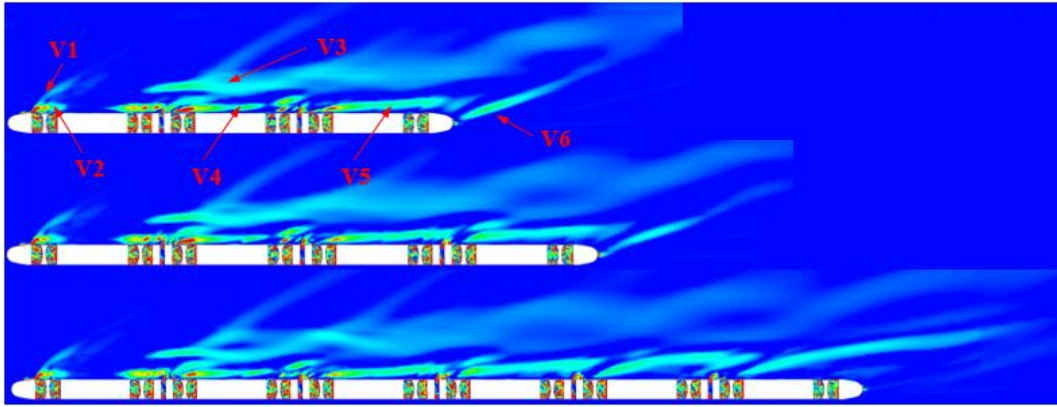
Fig. 18. Vorticity of horizontal section (z=1m) of trains with different marshalling length.

change. As can be seen from the figure, V5 and V6 near the tail-car change significantly. When the marshalling length increases, V5 gradually moves away from the tail-car body, while V6 gradually develops in the z direction. By comparing the vorticity around the body of the four intermediate cars of the six marshalling train, it can be seen that from M1-car to M4-car, the vortex gradually leaves the body, and the vorticity intensity near the body of intermediate cars gradually decreases.

6. CONCLUSION

1. The marshalling length has a significant influence on trains running under crosswind. At a crosswind velocity of 30m/s, 34% difference in F_s of the tail-car of a 6-marshalling train compared to a 3-marshalling. The overturning moment differs by 22.8%.

2. No matter how length the marshalling is, the head-car and M1-car have the same aerodynamic characteristics. At the same crosswind velocity, the order of F_s and M_o of each car is head-car middle-car and tail-car, the F_s and M_o of the M2-car of the 4-marshalling and 6-marshalling trains are essentially the same. When the marshalling length increase, the F_s and M_o of the tail-car decreases.

3. The thickness of the surface boundary layer on the windward side of the tail-car decreases with the increase of marshalling length. As the marshalling length increases, the intensity of the vortex near the tail-car decreases, the separation point at the tail-car's nose keeps moving away from the nose, and vortices V3, V5 and V6 on the leeward side of the tail-car move far away from the car body, gradually becoming larger. The increase of marshalling length does not change the flow field around the head-car and the first intermediate car, but has a significant impact on the flow field around the tail-car.

4. Numerical calculation results of crosswind aerodynamic performance of urban EMUs with different marshalling lengths show that different marshalling lengths have little effect on the aerodynamic performance of the head-car and the M1-car. But the impact on the tail-car is particularly obvious. For research focusing on the tail-car, the real marshalling length should be used, as far as possible.

REFERENCES

Bell, J. R., D. Burton, M. C. Thompson, A. H. Herbst and J. Sheridan (2015). Moving model analysis of the slipstream and wake of a high-speed train. *Journal of Wind Engineering and Industrial Aerodynamics* 136, 127-137.

Bell, J. R., D. Burton, M. C. Thompson, A. H. Herbst and J. Sheridan (2014). The effect of length to height ratio on the wake structure and surface pressure of a high-speed train. *19th Australasian Fluid Mechanics Conference (AMFC),* Melbourne, Australia. 8-11.

Chang, C., T. Li, D. Qin and J. Y. Zhang (2022). On the Scale Size of the Aerodynamic Characteristics of a High-Speed Train. *Journal of Applied Fluid Mechanics* 15(1), 209-219.

Chiu, T. W. and L. C. Squire (1992). An experimental study of the flow over a train in a crosswind at large yaw angles up to 90. *Journal of Wind Engineering and Industrial Aerodynamics* 45(1), 47-74.

EN14067-6 (2010). Railway applications - aerodynamics -part 6: requirements and test procedures for cross wind assessment

Guo, D. L., K. M. Shang, Y. Zhang, G. W. Yang and Z. X. Sun (2016). Influences of affiliated components and train length on the train wind.

Acta Mechanica Sinica 32(2), 191-205.

Jia, L. R., D. Zhou and J. Q. Niu (2017). Numerical calculation of boundary layers and wake characteristics of high-speed trains with different lengths. *Plos one* 12(12): e0189798.

Li, T., Z. Y. Dai, M. G. Yu and W. H. Zhang (2021). Numerical investigation on the aerodynamic resistances of double-unit trains with different gap lengths. *Engineering Applications of Computational Fluid Mechanics* 15(1), 549-560.

Li, T., H. Hemida, J. Y. Zhang, M. Rashidi and D. Flynn (2018). Comparisons of shear stress transport and detached eddy simulations of the flow around trains. *Journal of Fluids Engineering* 140(11), 111108.

Li, T., J. Y. Zhang, M. M. Rashidi and M. G. Yu (2019) On the Reynolds-averaged Navier-Stokes modelling of the flow around a simplified train in crosswinds. *Journal of Applied Fluid Mechanics* 12(2), 551-563.

Liu, T. H., Z. H. Jiang, W. H. Li, Z. J. Guo, X. D. Chen, Z. W. Chen and S. Krajnovic (2019). Differences in aerodynamic effects when trains with different marshalling forms and lengths enter a tunnel. *Tunnelling and Underground Space Technology* 84, 70-81.

Liu, T. H., Z. W. Chen, X. S. Zhou and J. Zhang (2018). A CFD analysis of the aerodynamics of a high-speed train passing through a windbreak transition under crosswind. *Engineering Applications of Computational Fluid Mechanics* 12(1), 137-151.

Martínez, A., E. Vega, J. Gaite and J. Meseguer (2008). Pressure measurements on real high-speed trains travelling through tunnels. *Proceedings of BBAA VI International Colloquium on Bluff Bodies Aerodynamics & Applications, Milano, Italy*. 20-24.

Mohebbi, M. and M. A. Rezvani (2018). The Impact of Air Fences Geometry on Air Flow around an ICE3 High Speed Train on a Double Line Railway Track with Exposure to Crosswinds. *Journal of Applied Fluid Mechanics* 11(3), 743-754.

Muld, T. W., G. Efraimsson and D. S. Henningson (2014). Wake characteristics of high-speed trains with different lengths. *Proceedings of the Institution of Mechanical Engineers, Part F: Journal of Rail and Rapid Transit* 228(4), 333-342.

Patankar, S. V. (1985). A Calculation Procedure for Two Dimensional Elliptic Situations. *Numerical Heat Transfer* 14, 409-425.

Qi, Y. H. and L. Zhou (2020). The Fuxing: The China Standard EMU. *Engineering* 6(3), 227-233.

Raithby, G. D. and G. E. Schneider (1979). Numerical Solution of Problems in Incompressible Fluid Flow; Treatment of the Velocity-Pressure Coupling. *Numerical Heat Transfer* 2(2), 417-440.

Ricco, P., A. Baron and P. Molteni (2007). Nature of pressure waves induced by a high-speed train travelling through a tunnel. *Journal of Wind Engineering and Industrial Aerodynamics* 95(8), 781-808.

Tian, H. Q. (2019). Review of research on high-speed railway aerodynamics in China. *Transportation Safety and Environment* 1(1), 1-21.

Van Doormaal J. P. and G. D. Raithb (1984) Enhancements of the SIMPLE Method for Predicting Incompressible Fluid Flows. *Numerical Heat Transfer* 7, 147-163.

Zhang, J., K. He, X. Xiong, J. Wang and G. Gao (2017). Numerical simulation with a DES approach for a high-speed train subjected to the crosswind. *Journal of Applied Fluid Mechanics* 10(5), 1329-1342.